

Compact Integration of Optical Sources and Detectors on SOI for Optical Interconnects Fabricated in a 200 mm CMOS Pilot Line

Thijs Spuesens, Fabien Mandorlo, Pedro Rojo-Romeo, Philippe Régreny, Nicolas Olivier, Jean-Marc Fedeli, and Dries Van Thourhout

Abstract—As the demand for bandwidth increases, optical interconnects are coming closer and closer to the chip. Optical interconnects on silicon-on-insulator (SOI) are desirable as this allows for integration with CMOS and the mature processing can be used for photonic integrated circuits. A heterogeneous integration process can be used to include III-V active optical components on SOI. For dense integration compact sources and detectors are required, but they typically need different epitaxial structures to be efficient which limits the integration density. We propose to use an epitaxial structure, which contains both the layers for a laser and for a detector, hereby enabling very compact integration of sources and detectors. Microdisk lasers and waveguide detectors using this epi were completely fabricated in a 200 mm CMOS pilot line and the results are discussed here.

Index Terms—Heterogeneous integration, microdisk laser (MDL), optical interconnect, photonic integration, silicon-on-insulator (SOI), waveguide detector.

I. INTRODUCTION

THE INCREASE of computational power in multicore CPUs comes together with a tremendous increase in required bandwidth for on-chip interconnects. Until now electrical interconnects can still keep up the pace, but in the near future physical limits will be reached and new types of interconnects are required. Optical interconnects do not suffer from a bandwidth length tradeoff as electrical interconnects do [1]. Therefore, it is believed that optical interconnects might form a good alternative to electrical interconnects. Silicon

photonics is considered as an interesting platform for these optical interconnects because of the possibility to realize complex and compact optical networks and the CMOS compatible fabrication process.

To realize an optical interconnect circuit, active components such as lasers, modulators and detectors are required. Several types of silicon modulators have already successfully been demonstrated [2]–[4]. Despite several efforts [5]–[7] efficient light generation in silicon is still not possible. Also, detectors cannot be made in silicon at telecom wavelengths. Therefore, to integrate sources and detectors on an silicon-on-insulator (SOI) platform other types of materials are required such as Germanium (Ge), which can be epitaxially grown on silicon [8], or III-V materials, which can be integrated with SOI by means of an adhesive or molecular bonding process [9]. Several types of lasers [10]–[12] and detectors [13]–[16] have already been successfully demonstrated on SOI.

However, for the use of optical interconnects in practical solutions it is desirable to be able to place the optical transmitters, modulators and receivers anywhere on the optical chip in a compact area. If for instance a bidirectional link is required, a compact transceiver block consisting of a laser or modulator and detector is needed. This asks for an integration scheme that allows these different structures to be processed in close proximity. Probably the most simple solution is to use the III-V epitaxial structure of the laser also for the detector, but this requires long detectors to achieve an acceptable responsivity and this limits the speed of the detector [17]. Separate III-V dies for lasers and detectors can be bonded, which ensures good performance of the devices, but then the lasers and detectors need to be spatially separated and thus the integration density is limited [18]. A configuration with off-chip lasers and on-chip ring based silicon modulators together with Ge photodetectors can be used for dense integration [4]. However, the insertion loss of these modulators is typically in the order of 6–10 dB. Therefore, the off-chip laser sources can only be shared over a few modulators. Moreover, because the sources are shared, they cannot be turned off and this results in a poor power budget.

In this paper, we propose an epitaxial structure, which contains both the layers for a laser and for a detector. This enables dense integration of lasers and detectors with a very limited amount of processing steps. Furthermore, by using a microdisk laser structure and a short waveguide detector, low footprints of 140 μm^2 for the laser and 450 μm^2 for the detector can be achieved.

Manuscript received December 22, 2011; revised February 13, 2012; accepted February 13, 2012. Date of publication March 05, 2012; date of current version April 06, 2012. This work was supported by the European FP7 ICT WADIMOS Project. The work of T. Spuesens was supported by the Institute for the Promotion of Innovation through Science and Technology (IWT) under a specialization grant.

T. Spuesens and D. Van Thourhout are with the INTEC Department, Ghent University-imec, 9000 Ghent, Belgium (e-mail: thijs.spuesens@intec.ugent.be; dries.vanhourhout@intec.ugent.be).

F. Mandorlo is with the Institut National des Sciences Appliquées de Lyon (INSA), 69621 Villeurbanne Cedex, France.

P. Rojo-Romeo and P. Regreny are with the Institut des Nanotechnologies de Lyon (INL), INL Unité Mixte de Recherche (UMR) 5270, Centre National de la Recherche Scientifique (CNRS), Ecole Centrale de Lyon, Université de Lyon, F-69134 Lyon, France.

N. Olivier and J.-M. Fedeli are with the Commissariat à l’Energie Atomique-Laboratoire d’Electronique de Technologie de l’Information (CEA-LETI), Minatec, 308054 Grenoble, France.

Color versions of one or more of the figures in this paper are available online at <http://ieeexplore.ieee.org>.

Digital Object Identifier 10.1109/JLT.2012.2189871

TABLE I
EPITAXIAL STRUCTURE

Layer	Composition	Doping	Thickness
Detector P	InGaAs	P++ $1 \times 10^{19} \text{ cm}^{-3}$	100 nm
Detector nid	InGaAs	nid	400 nm
Detector/laser N	InP	N+ $5 \times 10^{18} \text{ cm}^{-3}$	80 nm
Tunnel junction	Q1.3	N++ $1 \times 10^{19} \text{ cm}^{-3}$	25 nm
Tunnel junction	Q1.3	P++ $2 \times 10^{19} \text{ cm}^{-3}$	25 nm
Laser diode P	InP	P+ $1 \times 10^{18} \text{ cm}^{-3}$	135 nm
SCH	Q1.2	nid	25 nm
3x QW	InAsP	nid	3x6 nm
3x barrier	Q1.2	nid	3x15 nm
SCH	Q1.2	nid	25 nm
Laser diode N	Q1.2	N $1 \times 10^{18} \text{ cm}^{-3}$	120 nm
Laser N contact	InP	N+ $5 \times 10^{18} \text{ cm}^{-3}$	95 nm

Epitaxial growth layer structure for the laser and detector.

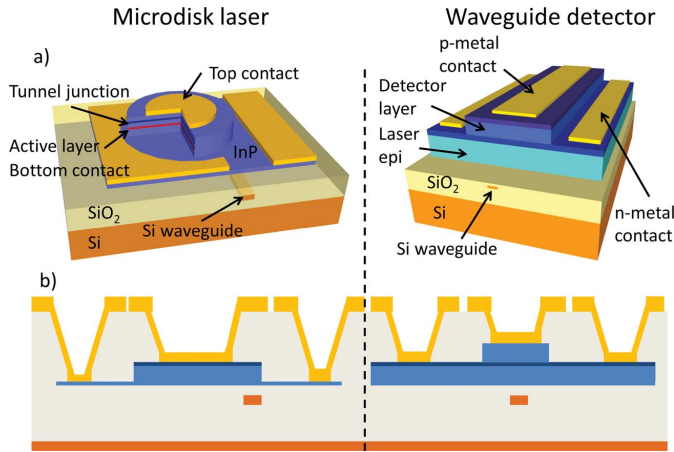


Fig. 1. (a) Overview and (b) cross-section of the microdisk and detector structure.

II. CONCEPT

Here we use a unique epitaxial structure, which contains both the epitaxial layers for the laser and the detector. In this configuration the detector layers are stacked on top of the laser. The details of the epitaxial structure are depicted in Table I. The thickness of the laser and detector layers is only 593 and 580 nm, respectively. Note that because the top contact layer of the laser and the bottom contact of the detector are shared the total thickness of the stack is only 1093 nm. If a laser is required at a certain position of the sample the detector layers can simply be removed by a wet etching step. On the other hand, if a detector is required the laser layers remain intact under the detector. This will not have a major impact on the detector performance as will be shown in Section II-B.

A. Micro Laser Design

A schematic representation of the microdisk laser is given in Fig. 1. The microdisk lasers have diameters in the range of 6 to 40 μm . The microdisk laser consists of a 493 nm thin disk cavity on top of a 95 nm thin InP bottom contact layer. The active layer consists of three compressively strained InAsP quantum wells and is surrounded by an n-doped layer on the bottom and a p-doped layer on top to form the diode structure. A tunnel junction is implemented on the p-side such that an n-type contact layer can be used instead of a heavily doped p-type contact layer, which would cause significant optical absorption. The tunnel

junction also ensures uniform current injection over the disk. The size of the top contact is a critical parameter as it should be small enough such that it will not cause significant absorption of the fundamental mode, while it should also be large enough to suppress the higher order radial modes that are present in disk cavities.

The light generated in the microdisk is coupled to an underlying waveguide through an evanescent coupling scheme. In order to have efficient coupling there should be sufficient phase matching between the fundamental mode in the disk cavity and the fundamental waveguide mode. While the height of the silicon waveguide is fixed to 220 nm in the used SOI platform, the width of the waveguide can be altered to achieve good phase matching. After the coupling section the waveguide is tapered back to 450 nm width and at both ends of the waveguide fiber couplers are used to couple out the light generated by the microdisk laser. Besides a good phase match there should also be sufficient overlap between the two modes. Therefore, both the lateral and vertical alignment of the waveguide with respect to the disk should be chosen carefully.

B. Detector Design

A schematic representation of the detector is shown in Fig. 1. It consists of a 400 nm i-InGaAs layer sandwiched between a 100 nm heavily doped p-type InGaAs top contact layer and an 80 nm n-type InP bottom contact layer that also served as the top contact of the laser. It has a waveguide type design where, similar to the microdisk laser, an evanescent coupling scheme is used to couple light from the underlying SOI waveguide to the detector. The phase matching condition is, compared to the laser, less critical for the detector because the light does not necessarily need to couple to a specific mode. The only requirement is that the modes to which the light is coupled have sufficient overlap with the absorption section of the detector. The waveguide under the detector has a width of 500 nm and a height of 220 nm. Detector lengths vary between 20 and 100 μm and the mesa has a width of 3.5 μm . The length variation was applied to find an optimum for both the responsivity and the bandwidth. A longer detector will enhance the responsivity, but at the same time the capacitance will increase which limits the bandwidth.

In order to calculate the optimal dimensions of the detector, the mode profiles and the amount of absorption, the detector structure was simulated using the commercial software package Fimmwave [19]. A slightly simplified structure was used to speed up the simulation. The laser diode P layer was combined with the tunnel junction and the laser diode N layer was combined with the SCH layer at the bottom of the structure. The top metal was taken over the full width of the detector mesa and the influence of the metal is therefore overestimated. A titanium metal layer was assumed with an absorption coefficient of 374 560 cm^{-1} . The absorption coefficient of the QWs and the InGaAs material was set to 5000 cm^{-1} . Because the height of the epitaxial structure of the detector including the laser layers, is around 1 μm and a practical mesa width is already a few micron, the effective index of the fundamental mode in the detector structure will be high compared to the fundamental mode in the silicon waveguide. As for efficient coupling a good phase match between the mode in the silicon waveguide and a certain

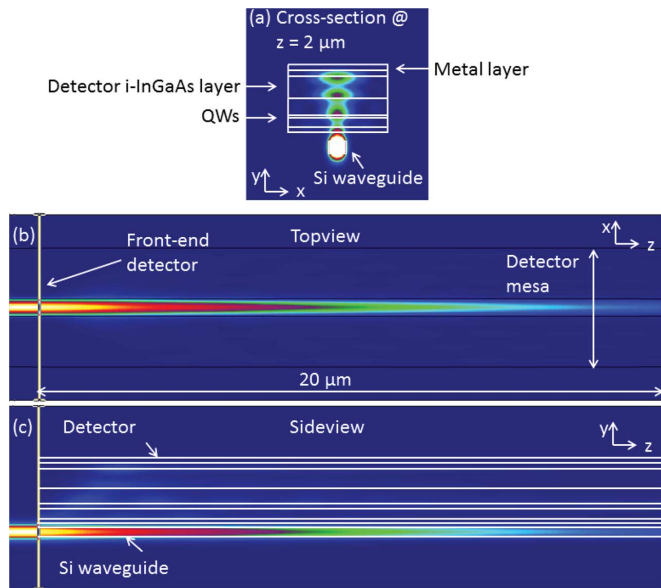


Fig. 2. (a) Detector mode profile at $2 \mu\text{m}$, which shows coupling to the fourth-order vertical mode. (b) Topview and (c) side view of the mode propagation and absorption in the detector.

detector mode is required, it is expected that efficient coupling will occur for higher order detector modes. Therefore, first an extensive mode list of the detector structure was built. Then, Fimmprop, the propagation module of Fimmwave, was used to inspect the coupling from the silicon waveguide to the detector structure and the amount of absorption in the detector. Fig. 2(a) shows the intensity profile in the detector after $2 \mu\text{m}$, it can be seen that the light couples mainly to the fourth-order vertical mode. The confinement factors are calculated to be 1.2% and 8.5% for the QWs and detector absorption layer, respectively. Fig. 2(b) and (c) shows the propagation and the absorption of the light where (b) is a top view of the detector and (c) is the sideview. Light is injected from the left side in a silicon waveguide of $1 \mu\text{m}$ length followed by the detector structure. It was found that for a detector length of $20 \mu\text{m}$ almost all of the input light is already absorbed. In this case however, the absorption in the laser QWs and the top metal also contribute to the total absorption. Therefore, to trace the influence of these layers other simulation runs were performed, where the absorption in specific layers was turned off. As expected the largest amount of absorption is for the case where there is QW, detector and metal absorption and is about 89% after $20 \mu\text{m}$. When the absorption in the QW layers is turned off, the total absorption is still 87% which indicates that the absorption in the QWs is very limited. It is difficult to determine the exact influence of the metal because when the absorption in the detector is turned off, the metal absorption will be overestimated as now all the light will reach the metal layer, while with detector absorption this is not the case. On the other hand, when the absorption in the metal is turned off, this will change the mode profiles, which makes it difficult to make comparisons. However, because the amount of absorption in the detector remained almost the same, with or without metal absorption, it is assumed the influence of the metal is limited. From these simulations we can conclude that there is sufficient coupling to the absorption layer of the detector

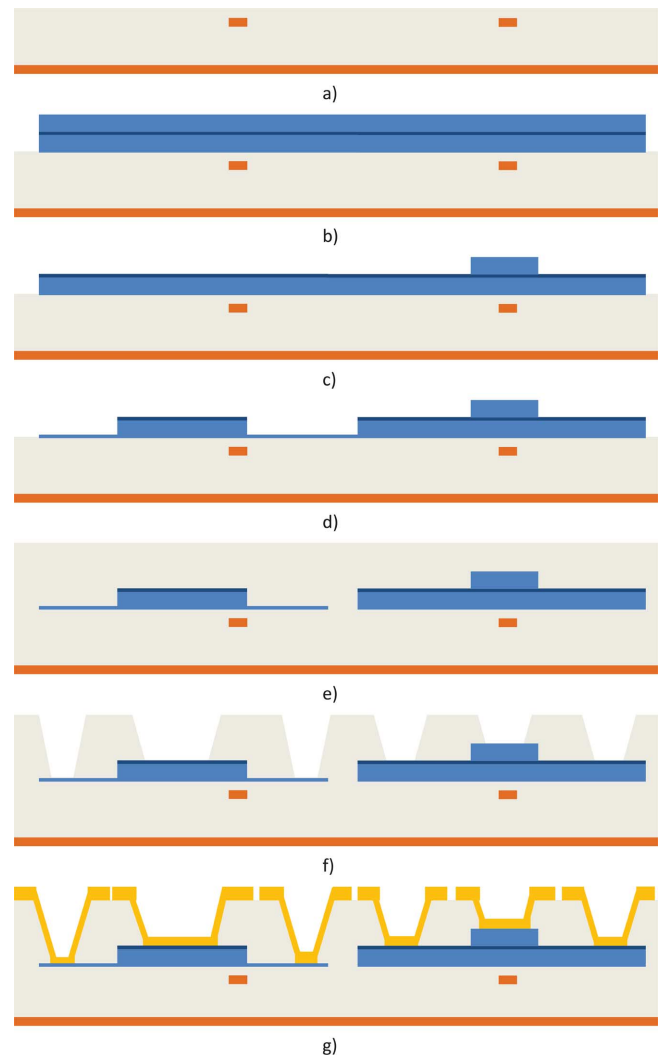


Fig. 3. Schematic overview of the processing steps of both the microdisk laser and the waveguide detector. (a) Patterning SOI wafer + oxide deposition + CMP. (b) Molecular bonding III-V dies + removing substrate and sacrificial layers. (c) Wet etch detector mesa. (d) Dry etch of microdisk and detector bottom contact. (e) Dry etch bottom contact layers + oxide deposition + CMP. (f) Oxide etch for vias. (g) Metal deposition + Metal etching.

and, because the overlap with the laser QWs is low, an efficient photodetector is feasible.

C. Processing

The process flow is depicted in Fig. 3. The epitaxial layers for the laser and detector are grown on a 2 inch InP wafer. The detector layers are grown first, such that after the bonding process the detector is positioned at the top. The patterned SOI wafer is planarized by depositing SiO_2 followed by chemical-mechanical polishing (CMP). To achieve heterogeneous integration of III-V material with SOI, unprocessed III-V dies or wafers, which are coated with a thin layer of SiO_2 , are bonded top side down on a 200 mm patterned SOI wafer by means of molecular bonding [9]. After the bonding process the InP substrate is removed down to an etch stop layer by mechanical grinding followed by chemical etching, so that only the desired epitaxial structure remains. The standard III-V processing steps

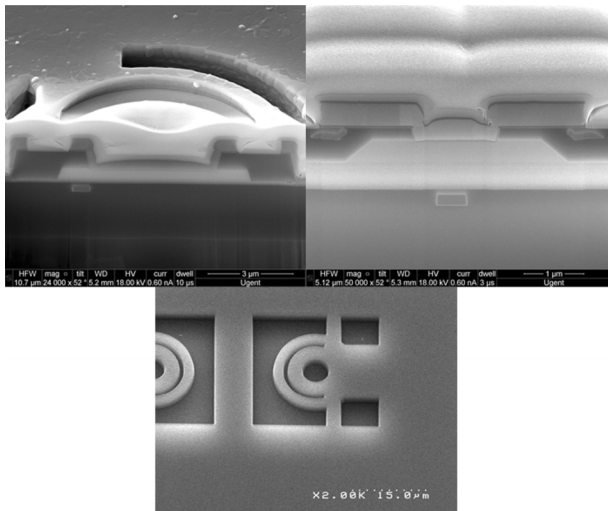


Fig. 4. Cross-sectional SEM images of the microdisk laser (top left) and detector (top right). The SEM image at the bottom is a top view of the vias of a microdisk laser and also shows the planarized surface.

are modified to comply with a 200 mm wafer scale CMOS environment. In particular, 248 nm DUV lithography is used to define the structures. All etching, oxide isolation layer deposition and metallization steps are performed at 200 mm wafer scale. The detector mesa is made by a wet etching step and then followed by two dry etching steps; one to make the detector bottom contact area and the disk cavity and another one to make the disk laser bottom contact area. SiO_2 is deposited as cladding layer and a CMP step is performed to planarize the surface. Then, to be able to contact the devices, all vias are etched in a single step where the III-V materials are used as an etch stop. The standard Ti/Pt/Au contacts cannot be used as gold is not allowed in a CMOS environment. Therefore a CMOS compatible Ti/TiN/AlCu metal stack is used [20]. This metal stack is full sheet deposited and after a lithography step, the metal stack is dry etched with a chlorine based solution. No annealing is performed on the wafers. The specific contact resistance is around $3 \times 10^{-5} \Omega \cdot \text{cm}^2$ for $5 \times 10^{18} \text{ cm}^{-3}$ n-InP and $6 \times 10^{-5} \Omega \cdot \text{cm}^2$ for $1 \times 10^{19} \text{ cm}^{-3}$ p-InGaAs. Cross-sectional SEM images of the microdisk laser and the photodiode and a top view SEM image of the planarized surface with the vias are shown in Fig. 4.

III. EXPERIMENTAL RESULTS AND DISCUSSION

Several wafers were processed with small variations in the bonding layer thickness. This is an important parameter as the coupling efficiency has an exponential dependence on the bonding layer thickness. The results discussed here are for a bonding layer thickness of ~ 130 nm. The coupling efficiency between the microdisk laser and the waveguide was calculated to be around 15% for this bonding layer thickness. Other critical parameters such as the lateral offset and width of the waveguide under the microdisk laser, top contact size and detector length were varied through a sweep in the design. Fiber couplers are used to collect the light generated by the laser and to inject light for the detector. The maximum efficiency of the fiber coupler was measured to be 27% at a wavelength of 1580 nm. The measured 3 dB bandwidth of the fiber coupler was found to be approximately 60 nm.

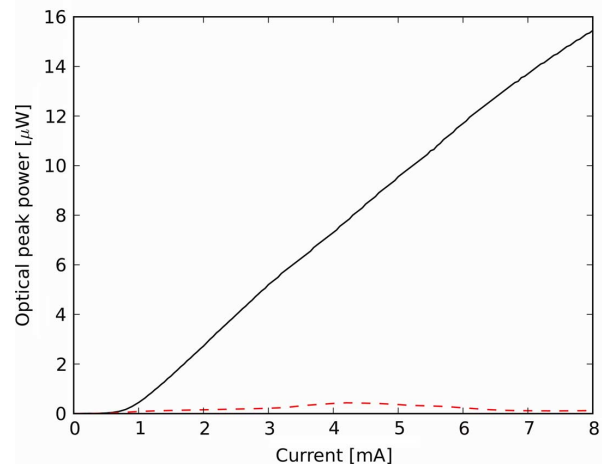


Fig. 5. LI curve in pulsed mode that shows unidirectional operation. Black solid line represents the left output and the red dashed line the right output of the microdisk laser. The power is the fiber coupled output power.

A. Microdisk Laser Performance

The results on the microdisk lasers discussed here are for disks with a diameter of $7 \mu\text{m}$. To measure the performance of the microdisk lasers first pulsed measurements were performed to avoid self heating effects. The microdisk lasers were electrically pumped by an ILX Lightwave LDP-3811 and the optical power and spectra were recorded with an HP 81532A power sensor and an Agilent 86140B optical spectrum analyzer, respectively. The result obtained for a pulsewidth of 100 ns and a duty cycle of 2% is shown in Fig. 5. The black solid line corresponds with the optical output from the clockwise mode measured at the left fiber coupler and the red dashed line with the output from the counterclockwise mode measured at the right fiber coupler. It is clear from this figure that the output is unidirectional as only the clockwise mode shows lasing behavior and almost no light is emitted in the opposite direction. Because the curve is unidirectional directly above the threshold current we believe this is caused by a stronger external reflection from one side than from the other, rather than being caused by intrinsic bistable behavior as reported in [21]. A threshold current of $600 \mu\text{A}$ and, after correction for the duty cycle, a peak optical power of $15.5 \mu\text{W}$ were measured in the fiber at an 8 mA drive pulse. Under these pulsed driving conditions the laser was lasing around a wavelength of 1536 nm. At this wavelength the fiber coupler efficiency was around 10% and therefore the peak optical power in the waveguide can be calculated to be $155 \mu\text{W}$.

The performance of the laser was also measured under CW operation where a Keithley 2400 was used as current source instead of the ILX Lightwave LDP3811 and the resulting LI curve is shown in Fig. 6(a). Again, the black solid line corresponds with the left fiber coupler and the red dashed line corresponds with the right fiber coupler. Clearly, both LI curves suffer from large oscillations, which are complementary with respect to each other. These oscillations between the clockwise and counterclockwise mode are caused by output light of the microdisk laser that is reflected back at the fiber couplers and interferes either constructively or destructively at the microdisk cavity. The variation in interference is a result of the change

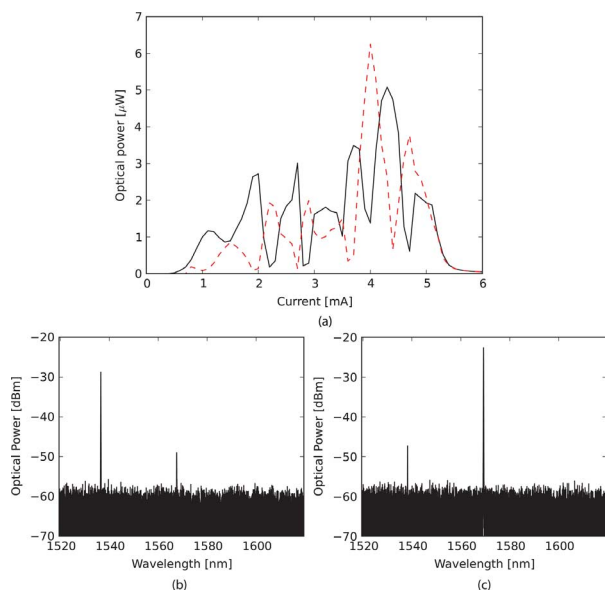


Fig. 6. (a) LI curve of both the left (black solid line) and right (red dashed line) output of the microdisk laser under CW operation, (b) spectrum at a drive current of 2.9 mA, and (c) spectrum at a drive current of 4 mA. The power is the fiber coupled output power.

in optical path length in the microdisk cavity under the influence of self-heating and the thermo-optic effect. When the drive current is changed, the refractive index of the cavity material changes but for the silicon waveguide it remains unchanged and this causes variation in the interference. The oscillations are larger than that of similar microdisks reported earlier in [12]. This is due to stronger interference with the reflected light from the fiber couplers as a result of the higher coupling efficiency between the disk and the waveguide. This higher coupling efficiency is a consequence of the better phase matching because of the thinner epitaxial stack of the microdisk compared to the microdisk reported in [12].

The maximum output power observed in CW operation for this laser is $6.25 \mu\text{W}$ measured in the fiber for a drive current of 4 mA. If the drive current is increased further, thermal rollover is observed. The jump in the LI curve around a drive current of 3.7 mA is also an indirect result of self heating. As the temperature in the cavity increases and the gain spectrum shifts towards longer wavelengths, mode hopping will occur. Spectra at two different drive conditions are shown in Fig. 6(b) and (c). The laser first lases around a wavelength of 1535 nm, but when the drive current is increased it hops to the next azimuthal mode around a wavelength of 1565 nm. The fiber coupler efficiency was 10% around 1535 nm and 20% around 1565 nm. As the fiber coupler efficiency is higher in the latter case, it results in higher power in the fiber. The maximum output power of $6.25 \mu\text{W}$ in the fiber thus corresponds with $31 \mu\text{W}$ in the silicon waveguide. The side mode suppression ratio is >25 dB at lower drive currents and >21 dB at drive currents above 3.7 mA.

The performance of the microdisk laser under elevated temperatures was also studied. The sample was heated by means of a Peltier element, under pulsed drive conditions to suppress self heating. The temperature was increased from 25°C to 70°C with the following steps 25°C , 30°C , 40°C , \dots , 70°C . The LI curves for the different ambient temperatures are displayed

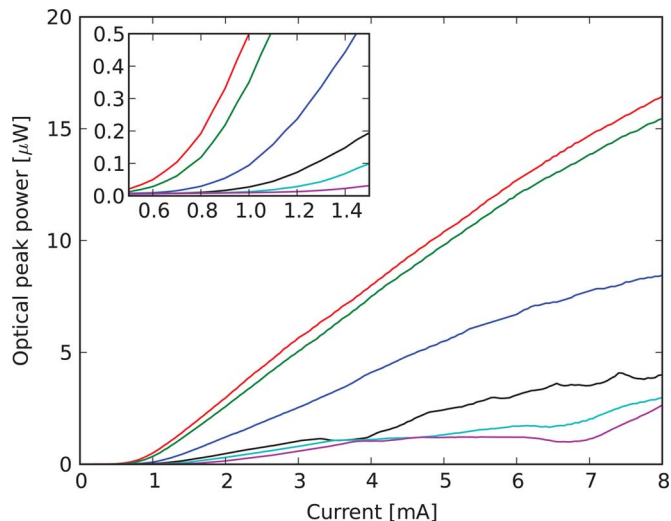


Fig. 7. LI curve under pulsed operation at elevated temperatures. The slope efficiency decreases and the threshold current (inset) increases at higher temperatures. The power is the fiber coupled output power.

in Fig. 7. As expected, the threshold current increases gradually with increasing temperatures as can be seen in the inset of Fig. 7 and the slope efficiency drops. At elevated temperatures under pulsed driving conditions the LI curve remains smooth and unidirectional, in contrast to the case where CW drive conditions were applied. Most likely this is because when the ambient temperature is changed, it affects both the silicon waveguide and the InP-based microdisk cavity, while the self heating effect in CW mode only heats up the disk cavity. As the thermo-optic coefficients for these materials are similar [22], [23], the phase difference between the output from the microdisk and the reflected light from the fiber coupler remains more or less constant and hence no oscillations are observed.

The characteristic temperature of the microdisk laser, T_0 , can be extracted by fitting the natural log of the threshold current versus the ambient temperature. A T_0 value of 53 K was found, which indicates that the laser is highly sensitive to temperature variations. Heterogeneously integrated lasers typically have high thermal resistance because they are bonded on SOI, and often also cladded, by SiO_2 or BCB which both have poor thermal conductivity. This problem becomes even worse for microdisk lasers because of their small footprint. The thermal resistance of these microdisk lasers was determined by measuring the wavelength as a function of ambient temperature ($d\lambda/dT$) and the wavelength change as a function of injected power ($d\lambda/dP$). The thermal resistance can now simply be calculated by $Z_T = (d\lambda/dT)^{-1}(d\lambda/dP)$. For $d\lambda/dT$ we found a value of 88.5 pm/K and for $d\lambda/dP$ we found 0.69 nm/mW. The thermal resistance Z_T then becomes 7.84 K/mW, which is, e.g., at least a factor of 3 higher compared to VCSELS of comparable dimensions on a GaAs substrate [24]. Therefore, in future devices special attention should be paid to improve the heat dissipation of the microdisk laser. For instance by adding a metal heat spreading layer as proposed in [21].

In order to tune the laser to the desired output wavelength a III-V ring heater around the disk can be used as demonstrated in [25]. This III-V ring was defined together with the disk and thus no extra processing steps were required. A microscope image of

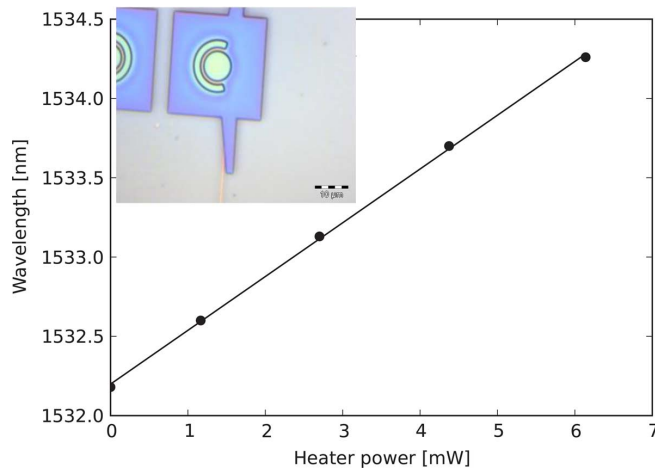


Fig. 8. Wavelength shift versus heater power for a III-V ring heater around a microdisk laser. Inset: microscope image of a microdisk cavity with a ring heater around it.

the ring heater is shown in the inset of Fig. 8. With the heater the laser can be trimmed around a certain azimuthal mode or it can be forced to work in a higher order azimuthal mode if the heater power is increased further. The efficiency of the heater can be deduced from Fig. 8 where the wavelength is plotted versus the heater power and is 0.32 nm/mW.

In order to make efficient optical links the bandwidth of the microdisk laser should be sufficiently large such that the dissipated energy per bit is low. The small-signal modulation of a microdisk laser was measured using an HP 83420A Lightwave test system. The result is shown in Fig. 9. The microdisk laser was biased at 1, 1.5, and 1.9 mA with a Keithley 2400 and it was lasing around a wavelength of 1532 nm. As can be seen from the figure, a 3 dB bandwidth of 7.8 GHz was achieved for a bias of 1.9 mA. Because the output power in the fiber is relatively low due to the off-target peak efficiency of the fiber couplers, the large signal modulation could not be measured yet. However, it is likely that the reflections from the fiber couplers will have a negative effect. The temperature in the microdisk cavity will slowly fluctuate depending on the length of trailing ones and zeros and, as explained above, result in switching between the clockwise and counterclockwise mode. This will become visible as amplitude noise in the signal.

B. Waveguide Detector Performance

First the current-voltage characteristics with and without illumination were measured. A Tunic Plus 1500–1640 tunable laser was used as a source and a Keithley 2400 was used to measure the current-voltage relation. The results discussed here are for detector lengths of 20 and 80 μm . Fig. 10 shows the IV curves of both 20 (red) and 80 (μm) long detectors. The dark current was measured to be 1.9 μA for a 20 μm long detector and 7.9 μA for an 80 μm long detector at a reverse bias of 2 V. Typically the dark current for InGaAs based detectors is in the range of a few nano Amperes, so the measured dark current is an order of magnitude larger than the typical value. Most likely this is caused by not timely passivating the structure, resulting in a lot of surface states and therefore high surface recombination. By careful passivation the dark current is expected to reduce. The optical power from the tunable laser

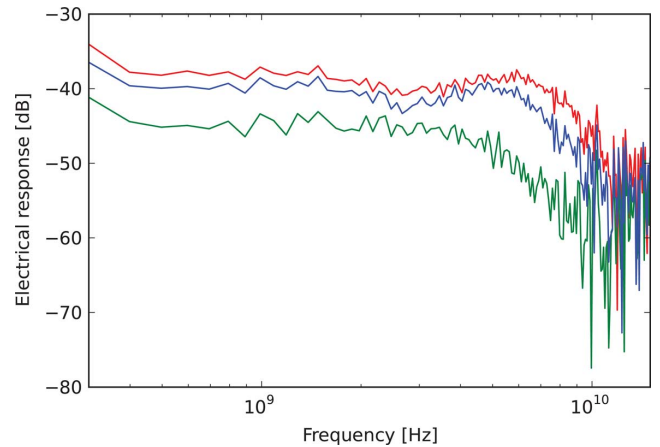


Fig. 9. Electrical response of the microdisk laser under a bias of 1 mA (green), 1.5 mA (blue), and 1.9 mA (red).

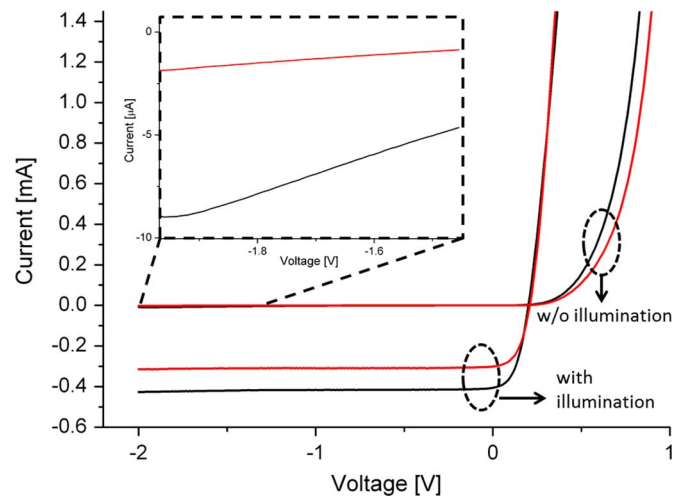


Fig. 10. IV characteristic of a 20 μm (red line) and 80 μm (black line) long detector.

source was measured just before the fiber couplers and was 2.88 mW at 1550 nm. With a fiber coupler efficiency of 15% at this wavelength the power in the waveguide was 432 μW . This optical power generates a photocurrent of 310 and 420 μA for a 20 and 80 μm long photodetector, respectively, which corresponds with responsivities of 0.71 and 0.97 A/W. From the slopes of the IV curves under forward bias it was found that the series resistance is $\sim 100 \Omega$ for both devices.

The frequency response of the detectors was measured with an Agilent N4373B Light Component Analyzer (LCA). The modulated optical output from the LCA was coupled into the SOI waveguide via a fiber coupler, while the electrical input from the LCA was connected to the detector via a bias-tee to measure electrical RF response. A Keithley 2400 voltage source was used to apply a reverse bias and to monitor the average photocurrent. Fig. 11 shows the frequency response for both detector structures. The 3 dB bandwidth under a reverse bias of -1.5 V was around 9 GHz for the 80 μm long detector and around 16 GHz for the detector with a length of 20 μm . The lower bandwidth for the 80 μm long detector can be explained by the larger capacitance following from an increased mesa area. It should be noted that the interference shape in Fig. 11

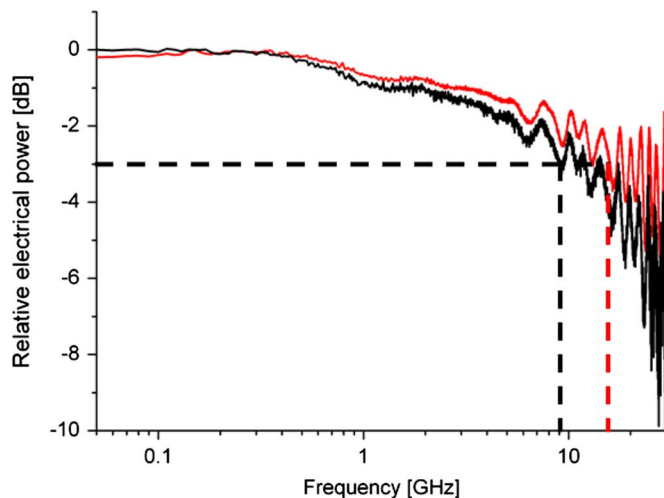


Fig. 11. Electrical response of a 20 μm (red line) and 80 μm (black line) long detector at a reverse bias of 1.5 V.

is similar for both detectors. This is most likely caused by a not perfect calibration of the network analyzer and therefore not perfect de-embedding of the electrical cables and the bias-tee. From the measured series resistance and 3 dB bandwidth we find that the capacitance of the detector including the pads is in the order of a few hundred fF. This is in good agreement with the calculated values for the parasitic capacitance of the detector which are 20 and 80 fF for the 20 and 80 μm long detector, respectively.

IV. CONCLUSION

We proposed a unique epitaxial structure, which contains both the layers for a laser and for a detector. Hereby it becomes possible to integrate lasers and detectors in close proximity, which is desirable for practical interconnects.

A microdisk laser and waveguide detector using this epitaxial structure were completely fabricated in a 200 mm CMOS pilot line and demonstrated here.

REFERENCES

- [1] D. Miller, "Device requirements for optical interconnects to silicon chips," *Proc. IEEE*, vol. 97, no. 7, pp. 1166–1185, Jul. 2009.
- [2] L. Liao, A. Liu, J. Basak, H. Nguyen, M. Paniccia, D. Rubin, Y. Chetrit, R. Cohen, and N. Izhaky, "40 Gbit/s silicon optical modulator for high-speed applications," *Electron. Lett.*, vol. 43, no. 22, 2007.
- [3] F. Y. Gardes, A. Brimont, P. Sanchis, G. Rasigade, D. Marris-Morini, L. O'Faolain, F. Dong, J. M. Fedeli, P. Dumon, L. Vivien, T. F. Krauss, G. T. Reed, and J. Martí, "High-speed modulation of a compact silicon ring resonator based on a reverse-biased pn diode," *Opt. Expr.*, vol. 17, no. 24, pp. 21986–21991, Nov. 2009.
- [4] L. Chen, K. Preston, S. Manipatruni, and M. Lipson, "Integrated GHz silicon photonic interconnect with micrometer-scale modulators and detectors," *Opt. Expr.*, vol. 17, no. 17, pp. 15248–15256, Aug. 2009.
- [5] L. Pavesi, L. Dal Negro, C. Mazzoleni, G. Franzò, and F. Priolo, "Optical gain in silicon nanocrystals," *Nature*, vol. 408, no. 6811, pp. 440–444, Nov. 2000.
- [6] H. Rong, R. Jones, A. Liu, O. Cohen, D. Hak, A. Fang, and M. Paniccia, "A continuous-wave Raman silicon laser," *Nature*, vol. 433, no. 7027, pp. 725–728, 2005.
- [7] J. Liu, X. Sun, R. Camacho-Aguilera, L. C. Kimerling, and J. Michel, "A Ge-on-Si laser operating at room temperature," *Opt. Lett.*, vol. 35, no. 5, pp. 679–681, 2010.

- [8] H. C. Luan, D. R. Lim, K. K. Lee, K. M. Chen, J. G. Sandland, K. Wada, and L. C. Kimerling, "High-quality Ge epilayers on Si with low threading-dislocation densities," *Appl. Phys. Lett.*, vol. 75, no. 19, p. 2909, 1999.
- [9] G. Roelkens, J. Van Campenhout, J. Brouckaert, D. Van Thourhout, R. Baets, P. R. Romeo, P. Regreny, A. Kazmierczak, C. Seassal, X. Letarte, G. Hollinger, J.-M. Fedeli, L. Di Cioccio, and C. Lagahe-Blanchard, "III-V/Si photonics by die-to-wafer bonding," *Materials Today*, vol. 10, no. 7–8, pp. 36–43, 2007.
- [10] H. Park, A. Fang, S. Kodama, and J. Bowers, "Hybrid silicon evanescent laser fabricated with a silicon waveguide and III-V offset quantum wells," *Opt. Expr.*, vol. 13, no. 23, pp. 9460–9464, Nov. 2005.
- [11] A. W. Fang, E. Lively, Y.-H. Kuo, D. Liang, and J. E. Bowers, "A distributed feedback silicon evanescent laser," *Opt. Expr.*, vol. 16, no. 7, pp. 4413–4419, Mar. 2008.
- [12] J. Van Campenhout, P. R. Romeo, P. Regreny, C. Seassal, D. Van Thourhout, S. Verstuyft, L. Di Cioccio, J.-M. Fedeli, C. Lagahe, and R. Baets, "Electrically pumped InP-based microdisk lasers integrated with a nanophotonic silicon-on-insulator waveguide circuit," *Opt. Expr.*, vol. 15, no. 11, pp. 6744–6749, May 2007.
- [13] J. Brouckaert, G. Roelkens, D. Van Thourhout, and R. Baets, "Compact InAlAs-InGaAs metal-semiconductor-metal photodetectors integrated on silicon-on-insulator waveguides," *IEEE Photon. Technol. Lett.*, vol. 19, no. 19, pp. 1484–1486, 2007.
- [14] H. Park, A. W. Fang, R. Jones, O. Cohen, O. Raday, M. N. Sysak, M. J. Paniccia, and J. E. Bowers, "A hybrid AlGaInAs-silicon evanescent waveguide photodetector," *Opt. Expr.*, vol. 15, no. 10, pp. 6044–6052, May 2007.
- [15] G. Masini, S. Sahni, G. Capellini, J. Witzens, and C. Gunn, "High-speed near infrared optical receivers based on Ge waveguide photodetectors integrated in a CMOS process," *Adv. Opt. Technol.*, vol. 2008, pp. 1–5, 2008.
- [16] D. Feng, S. Liao, P. Dong, N.-N. Feng, H. Liang, D. Zheng, C.-C. Kung, J. Fong, R. Shafihi, J. Cunningham, A. V. Krishnamoorthy, and M. Asghari, "High-speed Ge photodetector monolithically integrated with large cross-section silicon-on-insulator waveguide," *Appl. Phys. Lett.*, vol. 95, no. 26, p. 261105, 2009.
- [17] G. Roelkens, D. Van Thourhout, R. Baets, R. Nötzel, and M. Smit, "Laser emission and photodetection in an InP/InGaAsP layer integrated on and coupled to a silicon-on-insulator waveguide circuit," *Opt. Expr.*, vol. 14, no. 18, pp. 8154–8159, Sep. 2006.
- [18] J. Van Campenhout, P. Binetti, P. R. Romeo, P. Regreny, C. Seassal, X. J. M. Leijtens, T. De Vries, Y. S. Oei, R. P. J. Van Veldhoven, R. Nötzel, L. Di Cioccio, J.-M. Fedeli, M. Smit, D. Van Thourhout, and R. Baets, "Low-footprint optical interconnect on an SOI chip through heterogeneous integration of InP-based microdisk lasers and microdetectors," *IEEE Photon. Technol. Lett.*, vol. 21, no. 8, pp. 522–524, 2009.
- [19] Photon Design, "Integrated optics software fimmwave," 2011.
- [20] L. Grenouillet, A. Bavencove, T. Dupont, J. Harduin, P. Philippe, P. Regreny, F. Lelarge, K. Gilbert, P. Grosse, and J. Fedeli, "CMOS compatible contacts and etching for InP-on-silicon active devices," in *Proc. 6th IEEE Int. Conf. Group IV Photon. (GFP)*, 2009, pp. 196–198.
- [21] L. Liu, R. Kumar, K. Huybrechts, T. Spuesens, G. Roelkens, E. J. Geluk, T. De Vries, P. Regreny, D. Van Thourhout, R. Baets, and G. Morthier, "An ultra-small, low-power, all-optical flip-flop memory on a silicon chip," *Nature Photon.*, vol. 4, no. 3, pp. 182–187, 2010.
- [22] G. Ghosh, *Handbook of Thermo-Optic Coefficients of Optical Materials With Applications*. Waltham, MA: Academic Press, 1998, vol. 5.
- [23] F. G. Della Corte, G. Cocorullo, M. Iodice, and I. Rendina, "Temperature dependence of the thermo-optic coefficient of InP, GaAs, and SiC from room temperature to 600 K at the wavelength of 1.5 μm ," *Appl. Phys. Lett.*, vol. 77, no. 11, p. 1614, 2000.
- [24] A. Al-Omari and K. Lear, "Low current density, inverted polarity, high-speed, top-emitting 850 nm vertical-cavity surface-emitting lasers," *IET Optoelectron.*, vol. 1, no. 5, pp. 221–225, 2007.
- [25] L. Liu, T. Spuesens, G. Roelkens, D. Van Thourhout, P. Regreny, and P. Rojo-Romeo, "A thermally tunable III-V compound semiconductor microdisk laser integrated on silicon-on-insulator circuits," *IEEE Photon. Technol. Lett.*, vol. 22, no. 17, pp. 1270–1272, 2010.

Author biographies not included at authors' request due to space constraints.